



JGR Solid Earth

RESEARCH ARTICLE

10.1029/2018JB016626

Key Points:

- Geodetic measurements illuminate active deformation near the Rio Grande Rift and Colorado Plateau
- Deformation is greater within and directly west of the fault-defined RGR than to the east in the Great Plains
- The Colorado Plateau behaves as a nonrigid block with elevated strain rate accumulations at its margins

Supporting Information:

- Supporting Information S1
- Data Set S1

Correspondence to:

K. D. Murray,
kdm95@cornell.edu

Citation:

Murray, K. D., Murray, M. H., & Sheehan, A. F. (2019). Active deformation near the Rio Grande Rift and Colorado Plateau as inferred from continuous Global Positioning System measurements. *Journal of Geophysical Research: Solid Earth*, 124, 2166–2183. <https://doi.org/10.1029/2018JB016626>

Received 27 AUG 2018

Accepted 26 DEC 2018

Accepted article online 28 DEC 2018

Published online 27 FEB 2019

Active Deformation Near the Rio Grande Rift and Colorado Plateau as Inferred from Continuous Global Positioning System Measurements

K. D. Murray¹ , M. H. Murray² , and A. F. Sheehan³

¹Department of Earth and Atmospheric Sciences, Cornell University, Ithaca, NY, USA, ²Department of Earth and Environmental Science, New Mexico Institute of Mining and Technology, Socorro, NM, USA, ³Department of Geological Sciences, University of Colorado, Boulder, CO, USA

Abstract We used data from 333 continuous Global Positioning System stations, including 26 stations installed in 2006–2007 as part of a collaborative EarthScope experiment, to investigate how deformation is distributed near the Rio Grande Rift. Our previous analysis, using data from 2006 to 2010, was consistent with a nearly uniform east-west distributed extensional strain rate of ~ 1.2 ne/year (nanostain/year) along five profiles spanning a $\sim 1,000$ -km region. We built upon this analysis with additional Global Positioning System networks and longer time series of data spanning varying time ranges between 1993 and 2018. In all five east-west profiles, extensional strain rates are higher within and west of the fault-defined rift zone than to the east. There is an east-to-west increase in Central New Mexico from 0.7 ± 0.1 to 1.8 ± 0.8 ne/year that is significant at the 95% confidence level. We found elevated extensional and shear strain rates of over 10 ne/year along parts of the central Rio Grande Rift, particularly along the southeast edge of the Colorado Plateau along part of the Jemez lineament, as well as elevated dilatational strain rates and uplift above the Socorro magma body. Results from Euler pole analysis of Global Positioning System velocities for sites within the Colorado Plateau show nonrigid behavior with considerable deformation near the plateau margins and internal east-west extension. Our results suggest the Rio Grande Rift is actively deforming in an evolving tectonic environment.

1. Introduction

1.1. Motivation

Deformation across plate boundary zones is often widespread over regions of hundreds to thousands of kilometers (Bürgmann & Thatcher, 2013; Gordon, 1998); however, it is difficult to quantify the complex behavior of this active continental deformation. Large networks of continuous Global Positioning System (GPS) instruments and advances in processing techniques have begun to allow us to overcome difficulties of accurately measuring broadly distributed and complex patterns of present-day intracontinental deformation (e.g., Bürgmann & Thatcher, 2013; Segall & Davis, 1997). Globally, deformation tends to concentrate along large subduction zones and transform faults at plate boundaries, and much work has been done to better understand these areas and the complex processes that drive their deformation. However, intraplate tectonics, where processes such as slab foundering and mantle convection influence the continental interiors, are less well understood but are particularly important for the ongoing debate of how continents extend and rupture (England & McKenzie, 1982; Karlstrom et al., 2012; Reilinger et al., 2006; Ricketts et al., 2015, 2016; van Wijk et al., 2008).

The kinematics and dynamics of continental deformation in extensional areas such as the Rio Grande Rift (RGR; Figure 1) are controlled by a complex combination of lithospheric thinning, gravitational potential energy, temperature and density contrasts, rheology, asthenospheric flow, block rotations, fluids, and magmatism (e.g., Ballmer et al., 2015; Ricketts et al., 2014; van Wijk et al., 2008). Combinations of these forces can stress the entire plate, but deformation concentrates in certain areas where the crust is locally stressed (as in an active rifting model) and/or is particularly weak due to lithospheric heterogeneities, hydration, and other properties. Advances in space geodetic techniques, such as GPS, make it possible to accurately quantify the associated crustal deformation, but it is still unknown to what degree the observed deformation should be characterized by diffuse continuum

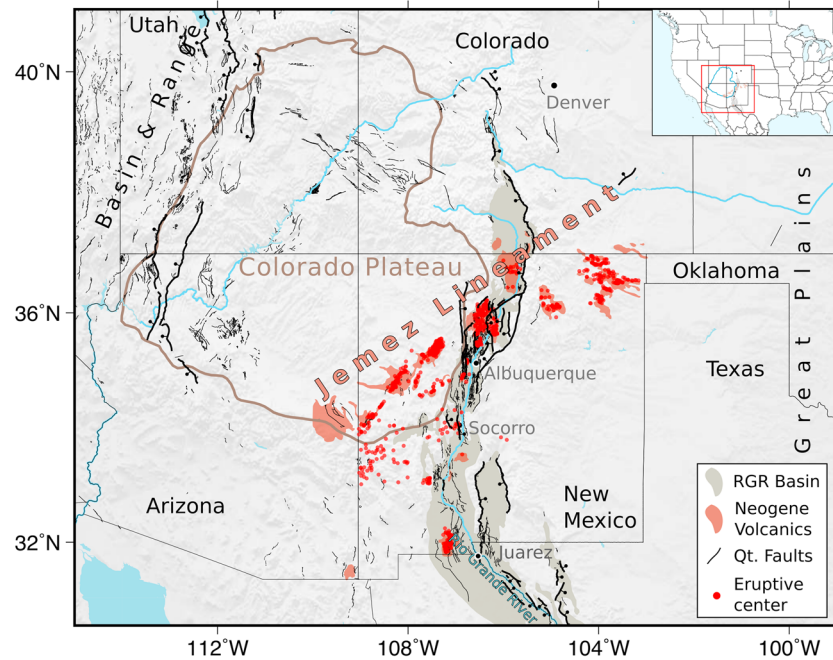


Figure 1. Map of the study area spanning the Great Plains in the east to the Basin and Range Province in the west. The Rio Grande Rift (RGR) basins (Hudson & Grauch, 2013) are shown in dark gray, the Colorado Plateau is outlined in brown, late Neogene volcanism is shown as red polygons with eruptive centers in New Mexico shown as red dots (from Geologic Map of New Mexico, New Mexico Bureau of Geology and Mineral Resources, 2003, scale 1:500,000), and Quaternary faults are shown as black lines (USGS, Quaternary Fault and Fold Database for the Nation, 2004). Large offset faults are shown as bold lines with bar and ball on footwall.

deformation or by motion of fault-bounded rigid subplates (Gordon, 1998; Thatcher, 2003, 2009). Difficulty in choosing the best model for the dynamics of continental deformation arises from the large contrasts between the brittle/elastic upper crust that deforms primarily along narrow weaknesses (Zoback & Zoback, 1989) and the rest of the lithosphere where strength and deformation depend primarily on temperature, fluid content, and composition (Evans & Kohlstedt, 1995; Thatcher, 2009). Studying deformation in low strain rate environments, such as the RGR, provides an opportunity to better understand how deformation is distributed and accommodated in the continental interior.

Slowly deforming environments such as the RGR are particularly difficult to study, due to the characteristically low signal-to-noise ratio of displacement measurements and long earthquake recurrence intervals, but they provide insights into complex continental dynamics and tectonic processes and the associated seismic hazards. Due to its slow net extension rate (less than 1 mm/year) and low volume of magmatism, the RGR has been proposed by many scientists to be a passive rift controlled by far-field forces (e.g., Gao et al., 2004). The cause of RGR opening is still a subject of debate, and the exact level and extent of current activity in the RGR is still unknown. Although several studies have speculated that the rift is not opening as fast today as it was in the Miocene (Kluth & Schaftenaar, 1994; Russell & Snelson, 1994), there is sufficient evidence to conclude that it is still tectonically and magmatically active. For example, previous studies have documented Holocene fault scarps (Machette, 2000), recent seismicity in and around the RGR (Sanford et al., 2002), ongoing basin subsidence (van Wijk et al., 2018), and the large active Socorro magma body (SMB)—one of the world's largest known magma bodies—which shows clear geodetically measurable active uplift and crustal deformation (Figure 4; Fialko & Simons, 2001; Finnegan & Pritchard, 2009). Ricketts et al. (2014) also summarized long-term and short-term extension rates (comparing geologic indicators to GPS data) and showed evidence for anomalously high, fluid-accelerated strain rates in the Quaternary in parts of the Albuquerque basin that were significantly faster than previously reported GPS-derived extension rates.

1.2. Geological and Geophysical Background

The RGR is commonly considered to be the eastern branch of the Basin and Range province and is defined physiographically by half-graben sedimentary basins trending north-south from the Southern Rocky Mountains to the southern section of the Basin and Range province. It is situated between the western margin of the Great Plains and the eastern margin of the Colorado Plateau (CP), which are both thought to be thick, semirigid crustal bodies as shown both geologically and geophysically (Chapin et al., 2004; Karlstrom et al., 2012; Keller & Cather, 1994; Kreemer et al., 2010). The average basin width of the RGR is approximately 50 km, with smaller basins in central and southern Colorado, widening to the south up to approximately 200 km in southern New Mexico where the rift diverges into multiple adjacent basins. RGR basins are bounded on the east and west by normal faults with Quaternary scarps (Machette, 2000). Structural trends of the RGR are generally consistent with structural trends from the Laramide orogeny, during which shallow subduction of the Farallon slab resulted in thrust-faulting and uplift. Many RGR structures are likely inherited from the Laramide orogeny in an inverted stress regime (Chapin et al., 1994). Structural observations of Neogene basins and accommodation zones, along with seismic-reflection studies, suggest that basin-bounding normal faults are listric and merge with older Laramide thrust faults at depth (Kellogg, 1999). The majority of the Quaternary faults in the RGR have low slip rates (0.03–0.2 mm/year; Machette, 2000; McCalpin et al., 2011). In spite of these low slip rates, paleoseismic studies, such as those done on the Sangre de Cristo Fault—a large basin-bounding normal-fault in south-central Colorado—have provided evidence for earthquakes of magnitude ~ 7.0 in the past 5,000 to 15,000 years (McCalpin, 1995). Recurrence intervals between such large earthquakes are commonly greater than 50 ka (Machette, 2000; Personius et al., 1999). There is an episodic pattern in rifting events, in which the rift undergoes periods of active extension (fault controlled or magma controlled), followed by periods of relative quiescence (Ebinger et al., 2013). Nonetheless, strong earthquakes (greater than magnitude 6.0) that rupture faults within the RGR occur once every approximately 750–1,000 years (Machette, 2000). More recent seismicity measured using the EarthScope Transportable Array and CREST (Colorado Rocky Mountains Experiment and Seismic Transects) temporary seismic networks from 2008 to 2010 shows mostly diffuse patterns (Nakai et al., 2017). Neogene faults in the northern section of the RGR are seismically active, although the most seismically active region of the RGR is in the central section from the San Luis basin to the southern part of the SMB—consistent with features of the western Jemez Lineament (Nakai et al., 2017).

The exact cause of extension and magmatism in the RGR has long been a subject of speculation and debate. Rifting has progressed episodically through a complicated relationship between changes in regional stress fields and resulting tectonomagmatic activity (Ebinger et al., 2013)—primarily controlled by plate-boundary processes. Near the end of the Laramide orogeny approximately 45 Ma, as convergence of the Farallon plate slowed, the slab began to break away and sink (Atwater & Stock, 1998; Chapin et al., 2004). Several studies have proposed that rifting is, at least in part, related to this sinking or roll-back of the subducting slab, which changed the regional stress field and induced asthenospheric upwelling (Atwater & Stock, 1998; Chapin et al., 2004; Humphreys et al., 2003; Ricketts et al., 2016). Others propose lithospheric and/or mantle heterogeneities inducing small-scale convection (van Wijk et al., 2008) or whole-mantle convection (Moucha et al., 2008) have affected rifting. Other ideas include internal deformation due to dynamic topography driven by variable asthenospheric upwelling, lithospheric delamination, and magmatic inflation (Channer et al., 2015; Karlstrom et al., 2012; Levander et al., 2011; Nereson et al., 2013).

After the last remnants of the Farallon plate and the Pacific spreading ridge had subducted approximately 18–17 Ma, the trend of North American plate motion near the plate boundary began to rotate to follow the Pacific plate westward (Atwater & Stock, 1998; Chapin et al., 1994; Zoback et al., 1981). This major tectonic change in Pacific-North American plate interaction resulted in large amounts of extension in the Great Basin, which expanded to cause a clockwise rotation of the CP microplate and possibly the onset of accelerated extension across the Rio Grande rift between 16 and 10 Ma (Chapin et al., 1994, 2004). Resulting magmatism and extension create weaknesses and heterogeneities in the lithosphere, which may drive more localized mantle processes and direct subsequent tectonic-magmatic activity through gravitational, buoyancy, and convective forces. Magmatism preceding extension of the RGR likely weakened the lithosphere and focused extension along the RGR (e.g., Baldrige et al., 2006). These tectonic changes also coincide with the end of the mid-Miocene volcanic lull near the RGR and the beginning of volcanism along the Jemez lineament. The least principal horizontal stress orientation rotated an additional $\sim 45^\circ$ between approximately 10 and 5 Ma—

roughly perpendicular to the fault strikes along the Jemez lineament (Eaton, 1979; Zoback et al., 1981). This is thought to have caused northwest expansion of the Basin and Range province, further rotation of the CP, and coincides with increased volcanism along the Jemez lineament (Chapin et al., 2004; Zoback et al., 1981).

1.3. Previous Geodetic Studies

Efforts to measure active crustal deformation of the RGR date back to 1970s. The earliest study was focused on looking for uplift from the Socorro magma body using leveling data (e.g., Reilinger & Oliver, 1976). Studies using trilateration data obtained near Socorro, New Mexico estimate within error of ± 1 mm/year of extension across the RGR with uncertainties too high to be conclusive (Prescott et al., 1979; Savage, 1983), and estimates from Very Long Baseline Interferometry data yield significantly higher strain rates of approximately 4–5 mm/year extension, which is higher than geologically derived strain rate estimates (Argus & Gordon, 1996). Argus and Gordon (1996) also found evidence for a clockwise rotation of the CP about a Euler pole in eastern Utah, but measurements were quite sparse and their uncertainties also high. Networks of continuous GPS in Colorado and New Mexico have grown considerably over the last two decades, making it possible to measure velocities with submillimeter accuracy given sufficient length time series and advanced processing techniques. Despite vast improvements over previously used methods, the GPS results have remained somewhat inconclusive. Kreemer et al. (2010) used a relatively sparse network with mostly short time series (<3 years) and focused on measuring deformation of the CP. They found that the majority of stations near the RGR and within the CP are moving westward at approximately 1 mm/year relative to stable North America but did not detect significant extension within the RGR itself. Rather they proposed that motion of the CP relative to the stable cratonic North America is partly accommodated by extension near the Jemez lineament—possibly related to rigid rotation of part of the CP. Berglund et al. (2012) added the analysis of an additional 26 stations that were installed in 2006 and 2007 as part of the EarthScope (<http://www.earthscope.org/>) funded RGR GPS experiment. They concluded that there is significant crustal motion in this area, but no obvious strain rate increase directly across the RGR. Rather, they found a gradual increase in velocities across the entirety of five approximately 1,000 km east-west profiles from the Great Plains to the western margin of the CP with an average strain rate of approximately 1.2 ± 0.2 nε/year (nanostain/year; Berglund et al., 2012). We extend and build upon these analyses by using a denser collection of GPS stations and >12 year time series, as well as an expanded analysis in order to determine the distribution of deformation along the RGR and better understand the processes driving deformation in the western United States continental interior.

2. Materials and Methods

2.1. GPS Networks and Processing

We used a combination of data from the Rio Grande Rift GPS network (Berglund et al., 2012), the greater Plate Boundary Observatory (PBO) network (pbo.unavco.org), the Continuously Operating Reference Network (CORS; www.ngs.noaa.gov), and the eastern part of the Mobile Array of GPS for NEvada Transtension (MAGNET) network (Blewitt et al., 2009; geodesy.unr.edu). Time series range from the early 1990s through early 2018. GPS velocities are from the Nevada Geodetic Laboratory through the University of Nevada Reno (Blewitt et al., 2018) and processed using JPL's GPS Inferred Positioning System (GIPSY)-OASIS II software and orbital products (Bertiger et al., 2010). GPS position time series and velocities were referenced to stable North America using the NA12 reference frame (Blewitt et al., 2013). These reference stations were chosen to represent the stable North American plate interior, away from plate boundary deformation to the west and postglacial rebound effects to the north, and show nearly zero internal deformation. It was realized through an iterative procedure that downweights or eliminates stations with high misfit values to determine if the a priori coordinates and velocities are consistent with the data from the reference sites.

The 26-station RGR GPS network was installed between 2006 and 2007 and was funded by the NSF EarthScope program (e.g., Berglund et al., 2012). This network was installed with the intent of studying extension across the RGR and includes five roughly E-W transects of GPS monuments spanning the RGR in Colorado and New Mexico. It consists primarily of shallow-drilled braced monuments, with seven single-mast monuments installed in areas where access did not permit full shallow-drilled braced monument installation. Data from these stations is collected daily using cellular telemetry or manually at more

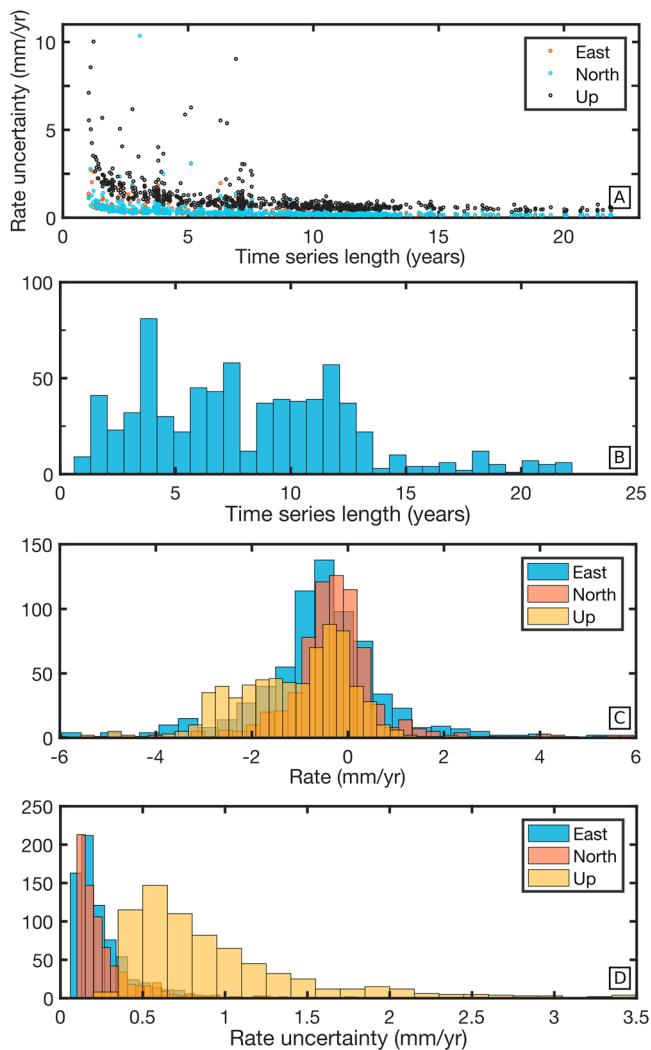


Figure 2. Statistics for all 672 sites in the study area. (a) Median Interannual Difference Adjusted for Skewness rate uncertainties with respect to the length of the time series. (b) Histogram of time series length. (c) Histogram of Global Positioning System rates of each component. (d) Histogram of rate uncertainties in each component.

remote sites. Data from this RGR network are now processed with the full PBO network, and daily position solutions are provided through UNAVCO in SINEX format.

The greater PBO network is the geodetic component of EarthScope and is funded by the National Science Foundation (www.earthscope.org). It consists of more than 1,000 continuously operating GPS stations mostly located within the United States. It is important in order to densify the local network near the RGR, as well as provide a reference frame at a larger scale to resolve phase ambiguities and stabilize position and velocity estimates of other sites within the local network. PBO stations are primarily high-quality receivers and monuments. The CORS network includes stations installed by other organizations such as local surveyors and is not extensively maintained or controlled by any particular organization. The stability of monuments in this network are generally lower quality than the PBO and RGR sites, but it has the advantage of having generally long time series of data available. Data are available through the National Geodetic Survey (NGS), which is operated by the National Oceanic and Atmospheric Administration (NOAA). The semicontinuous MAGNET network was deployed primarily to study the Basin and Range but offers a host of stations extending east into our field area and complements the other networks (Blewitt et al., 2009).

The quality of the GPS receivers and time series is variable (Figure 2). Given the low signal-to-noise ratio of the data near the RGR, we used strict criteria to only include the most reliable data in our analysis. Out of the approximately 672 available stations processed in the study area, we include 333 in the final analysis. We included only sites with horizontal rate uncertainty less than 0.5 mm/year and vertical rate uncertainty less than 1.5 mm/year, which eliminated the sites with the highest amounts of noise and/or significant transient behavior (i.e., deviations from a secular rate). Finally, the absolute value of the vertical rate was required to be less than 1 mm/year relative to NA12. This helped ensure sites affected by anthropogenic activity, such as extraction of groundwater and/or hydrocarbons or wastewater injection, are minimized (e.g., Argus et al., 2014). Eleven sites in Texas and Oklahoma, east of 102°W, whose uncertainties and rates otherwise meet the criteria, were also omitted from the final analysis due to suspected anthropogenic activity or unstable monuments. This is an area of high levels of industrial activity related primarily to oil and

gas production. Although many more sites could be included by relaxing some of the selection criteria—particularly by allowing for the absolute value of the vertical rates to be greater than 1 mm/year—rigorously separating tectonic signals from anthropogenic or regional uplift signals (e.g., Borsa et al., 2014) is beyond the scope of this project, which is focused on characterizing the broad-scale, primarily horizontal deformation patterns in the region.

2.2. Estimating GPS Velocities and Uncertainty

Given the low tectonic signal-to-noise ratio near the RGR, it is essential to carefully consider characteristics of noise present in the GPS time series. It is particularly important to recognize the colored noise components in geophysical data so that realistic uncertainties can be assigned to parameters estimated from them (Williams et al., 2004). We found rate uncertainties are underestimated by as much as an order of magnitude if we neglect the correlated noise and use a purely white noise model. We compared two approaches for estimating velocities and velocity uncertainties from the GPS time series: (1) solving for a secular rate, a seasonal periodicity and estimating uncertainties based on the spectral characteristics of the signal, and (2) estimating

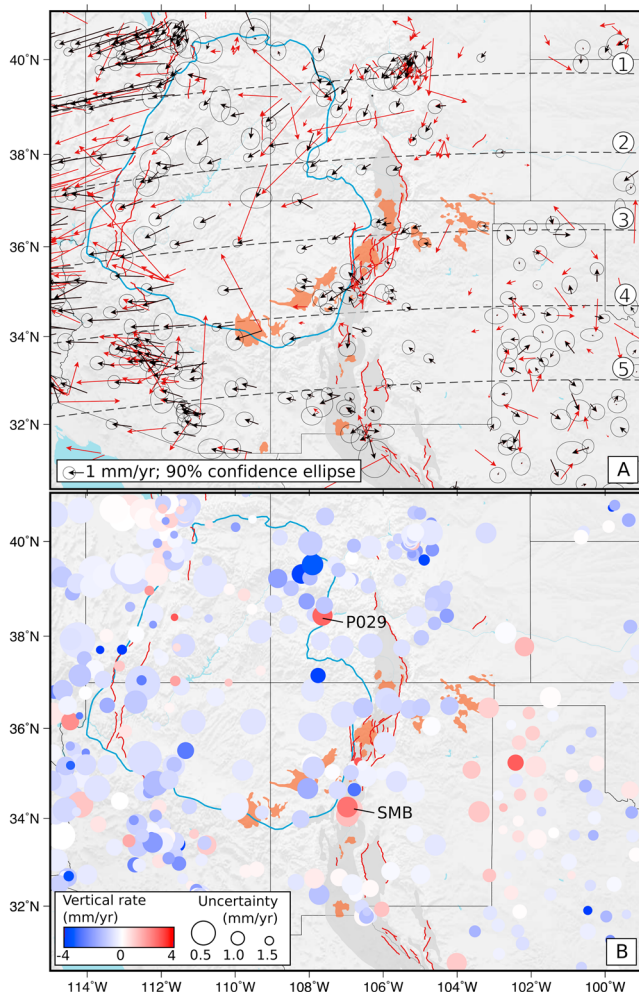


Figure 3. (a) Horizontal rates with 90% confidence error ellipses. East-west dashed lines labeled 1–5 are profiles shown in Figures 5 and 6. Vectors in red have been omitted from the analysis. (b) Vertical rates are shown in color scale (blue is subsidence, and red is uplift). The size of circles represents the vertical rate uncertainty (larger circles have lower uncertainty). Sites that were omitted from the analysis are also shown. (a and b) Colorado Plateau (CP) is outlined in blue, major Quaternary faults shown as red lines, late Neogene volcanics (Jemez lineament) shown in orange, and RGR basins shown in dark gray. SMB denotes location of the Socorro Magma Body.

velocities and uncertainties using the Median Interannual Difference Adjusted for Skewness (MIDAS) algorithm (Blewitt et al., 2016).

In the first approach, we modeled noise characteristics using the software package Hector (Bos et al., 2007). This package implements the Maximum Likelihood Estimation method, which estimates parameters of a time-dependent model of the GPS data and components of the covariance function simultaneously (Bos et al., 2013; Langbein & Bock, 2004; Langbein & Johnson, 1997; Williams et al., 2004). In order to increase processing speed, inversion of the full covariance matrix is avoided by creating a Toeplitz covariance matrix that is more easily inverted (Bos et al., 2013). We used a power-law model that represents a combination of random walk and flicker noise along with white noise (Langbein, 2012).

The second approach (the MIDAS algorithm) computes the median of slopes between all data pairs separated by 1 year—a variation of the Theil-Sen median trend estimator (Sen, 1968; Theil, 1950). Thus, time series length must be greater than 1 year such that at least one full cycle of periodic seasonal behavior, if it exists, is captured, and any transient signals can be distinguished from secular behavior. The differencing of pairs separated by a year minimizes effects with annual periodicity, but not other transient signals with different periodicity. This technique has been shown to be more robust against common noise structures such as step discontinuities, outliers, seasonality, skewness, and heteroscedasticity, than the more traditional least squares plus seasonal fitting (Blewitt et al., 2016). Similar to our first approach, uncertainty calculations are also more realistic with this algorithm than formal uncertainties from the least squares method, which do not account for long-term correlated noise characteristics.

Both of the approaches we compared agreed within a tenth of a millimeter in most cases. MIDAS results generally have slightly higher uncertainty values. For example, station RG01 has an east component velocity of 0.738 ± 0.105 mm/year derived using the first approach, and 0.789 ± 0.113 mm/year using MIDAS. Station PIE1 has an east component velocity of 0.391 ± 0.090 mm/year using the first approach and MIDAS east velocity of 0.334 ± 0.108 mm/year. For our analysis we chose the slightly more conservative result and use the velocities and uncertainties derived using the MIDAS algorithm.

2.3. Velocity Profiles

In order to test how velocities change across a large area from the Great Plains to the Basin and Range province and compare them to previous studies' results, we defined five east-west profiles (Figure 3). Each of the five profiles shows velocities for stations within 90 km of the profile. Velocities were projected onto the profile to show profile-parallel velocity. A weighted least-squares regression was done to fit a linear trend to the data in each profile. The slope of this linear trend is equivalent to the strain-rate across that distance.

We compared a model consisting of a single weighted regression that fits all data to the east of the RGR in the Basin and Range province (Figure 5) to a model consisting of three separate weighted regressions (two outside the fault-defined RGR and one inside the RGR if applicable) for all five profiles (Figure 6). There is a statistical trade-off between the improvement that is gained in a model by decreasing the weighted sum of squared residuals and the loss of degrees of freedom caused by the increase of number of parameters being estimated. Thus, we tested the quality of each regression using an *F* test (Stein & Gordon, 1984), in which two variances are compared based on the fit of the regression and the degrees of freedom associated with each set using the following equation:

Table 1
Results From Statistical *F* test

	Profile 1	Profile 2	Profile 3	Profile 4	Profile 5
	1-seg 2-seg	1-seg 2-seg	1-seg 3-seg	1-seg 3-seg	1-seg 3-seg
Number of stations	37	21	31	30	46
Degrees of freedom	35 33	19 17	29 25	28 24	44 40
χ^2	130.7 127.5	71.7 55.5	103.9 87.6	189.6 115.9	110.5 88.9
<i>F</i> statistic	0.41	2.48	1.16	3.82	2.43
<i>P</i> value	0.66	0.11	0.35	0.02	0.06

Note. Single-segment models are compared to segmented models for each profile. In each profile column, the left subcolumn shows values from the one-segment model, and the right subcolumn shows values from the three-segment model. Profile 2 has no data within the RGR faults and thus compares a one-segment model to a two-segment model. *P* value is less than 0.05 in profile 4, implying that the three-segment model is statistically better than the uniform model at the 95% confidence level.

$$F = \frac{(\chi_1^2 - \chi_2^2) / (df_1 - df_2)}{\chi_2^2 / df_2}, \quad (1)$$

where χ^2 is the weighted residual sum of squares for the *n*th data set and df_n is its respective number of degrees of freedom. Using the *F* statistic, a *p* value is found by creating a cumulative distribution function for *F*. The integral of the entire cumulative distribution function is 1, and the integral of the cumulative distribution function at values greater than or equal to our calculated *F* statistic gives the *p* value. This value represents the probability of obtaining an *F* statistic as extreme or more extreme than what we calculated given the two models. For 95% confidence, $\alpha = 0.05$. If the *p* value is large ($p > \alpha$), then the improvement in fit of the second model, compared to the first, is not statistically significant at the 95% confidence level. If the *p* value is small ($p < \alpha$), then the improvement in fit of the second model is statistically significant at the 95% confidence level (Table 1).

2.4. Strain Rate Field

In addition to strain rate calculations across the five profiles, we computed a two-dimensional strain rate field from velocity data. We implemented a two-step process by first interpolating the horizontal GPS vectors to an equally spaced grid (with a cell size of ~30 km²) using the implementation of Sandwell and Wessel (2016) and then computed the strain tensor and tensor invariants/eigenvalues at each grid cell. The interpolation method uses Green's functions for an elastic body and ensures realistic coupling between horizontal components. Strain rate is calculated as the gradient of the velocity field. We computed the strain rate tensor at each grid cell in a weighted linear least squares inversion in which each station is weighted by its distance to the center of the cell using a weighting matrix

$$W = \exp\left(\frac{-d^2}{2\beta^2}\right), \quad (2)$$

where *W* is the weighting factor, *d* is the distance in kilometers, and β is a constant that specifies how the influence of a station decays with distance (e.g., Cardozo & Allmendinger, 2009). We set $\beta = 40$ km such that neighboring cells contribute to more than two thirds of the calculation and decay rapidly at greater distances. Finally, we computed the tensor invariants and eigenvalues (Figures 7a–7c).

Because the two-step process used to estimate the strain tensor at each grid point is nonlinear, we performed Monte Carlo resampling to determine approximate uncertainties of the strain tensor and invariant/eigenvalue estimates. For each of the 1,000 trials, each station horizontal velocity component was randomly sampled using a normal probability distribution defined by the component value and one-sigma uncertainties. The trial results were then sorted, and an approximate one-sigma uncertainty was determined from the interval including 68.2% of the samples about the median value (Figures 7d–7f).

2.5. Euler Pole Analysis

Plate motion models, such as the NUVEL-1a (DeMets et al., 1994), characterize long term average plate motions and show that plates behave approximately like rigid bodies that rotate relative to each other

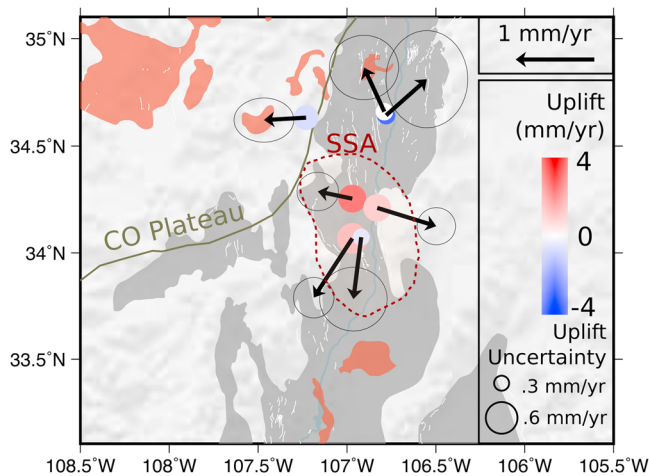


Figure 4. Rate map of the Socorro Magma Body (SMB) located in central New Mexico with horizontal rate vectors and 90% confidence ellipses, and vertical rates in color scale (blue is subsidence, and red is uplift). The dashed red line shows the outline of the Socorro Seismic Anomaly (SSA) as defined by Balch et al. (1997). Quaternary faults shown as white lines, late Neogene volcanics shown in orange, and RGR basins shown in dark gray.

(e.g., Larson et al., 1997; Norabuena et al., 1999). GPS velocity fields can be used to constrain present-day plate rotations by inverting velocity data to solve for Euler (angular velocity) parameters (Minster et al., 1974). In the Euler model, the motion of a plate on a sphere is characterized in three dimensions by its rotation about an imaginary axis through the center of the Earth. The three parameters estimated in this model are what constitute the Euler pole; they are the latitude and longitude of the point on the Earth's surface through which the Euler axis passes and the rotation rate, or angular velocity, at that point.

We used velocity estimates with respect to the NA12 reference frame to estimate Euler pole parameters for the CP. Following the method of Palano et al. (2010), in an Earth-centered-Earth-fixed (ECEF) Cartesian coordinate system, we defined a point p on the Earth's surface by its coordinates (x, y, z) . The forward problem for a velocity vector in geocentric coordinates $v(v_x, v_y, v_z)$ is given by

$$v = (\Omega \times p) = \begin{bmatrix} z\omega_y - y\omega_z \\ x\omega_z - z\omega_x \\ y\omega_x - x\omega_y \end{bmatrix} \quad (3)$$

where Ω is the model vector of Euler pole parameters $(\omega_x, \omega_y, \omega_z)$. We did a weighted linear least squares inversion to recover Ω given the velocities of the stations within the CP, then run the forward model to recover the modeled velocities and residuals (Figure 8). To estimate the Euler pole rotation of the CP, we used the horizontal velocities and their standard deviations of the 43 stations located within the physiographic region (Figure 8). Uncertainties on the pole location and rate were found using Monte Carlo trials where the value of each horizontal velocity component was randomly chosen from a normal distribution given by its estimated velocity and standard deviation. We performed 10,000 trials and selected the trials with the 9,500 smallest normalized root mean square residuals as a proxy for the 95% confidence limits on the Euler pole estimates. Alternatively, to test which sites follow the behavior of the geologically derived Euler pole, we run the forward model using this Euler pole and iteratively omit sites with high misfit values, rerunning the inversion until the best-fit group of 10 sites remain (see supporting information; Figure S2).

3. Results

3.1. Velocity Field

Horizontal velocities are generally low in the Great Plains and near the RGR (approximately 0.5 ± 0.1 mm/year) and steadily increase westward to approximately 1 mm/year into the CP before more dramatically increasing in the Basin and Range province to greater than 3 mm/year (Figure 3a). Sites in Colorado trend southward before rotating westward near the Jemez lineament. In contrast, velocities trend slightly northward in southern New Mexico before rotating westward near the Jemez lineament. K-means cluster analysis (MacQueen, 1967) results in roughly 4 clusters of stations based on their velocities, with a noteworthy division along the Jemez Lineament (see supporting information; Figure S1). There are a number of anomalies in the velocity field that deviate from general submillimeter, westward trends. The Socorro magma body in central New Mexico shows clear radial signals outward from its center (Figure 4). Other anomalies tend to concentrate near urban areas such as Denver, Albuquerque, and Juarez (Figure 1). Although our criteria for eliminating noisy sites eliminated the majority of sites affected by groundwater pumping and hydrocarbon production (Figure 3), many of the sites, particularly in areas like Texas, may be showing these effects. Many of the sites east of New Mexico are part of the CORS network, which is generally less reliable and more susceptible to monument/receiver instabilities and/or erroneous data management.

Vertical velocities are variable throughout the study area (Figure 3b). In general, most sites near and in the RGR show negative velocities (subsidence) around -0.5 to -1 mm/year, with the exception of sites near the Socorro magma body that are mostly uplifting up to ~ 4 mm/year, which is consistent with previous

Interferometric Synthetic Aperture Radar (InSAR) studies (Fialko & Simons, 2001; Finnegan & Pritchard, 2009; Figure 4).

Vertical velocities of sites within the CP and Rocky Mountain region show overall gradual subsidence (~ 1.5 mm/year). Sites on the northwest boundary of the CP and Basin and Range province transition to generally positive velocities between 0.1 and 1 mm/year, suggesting gradual uplift (Figure 3b). Site P029 (Figure 3b), at the northeast edge of the CP in the western San Juan Mountains, shows an anomalously high uplift rate ($\sim 2.1 \pm 0.5$ mm/year). Donahue et al. (2013) present geomorphic evidence for uplift and rapid incision rates of the Gunnison River in this area and propose that buoyant low-velocity mantle underlying these recently exhumed areas may be driving localized uplift. Similar to the horizontal velocities, vertical velocities are more variable between sites with larger uncertainties. For example, sites within Texas—an area of extensive hydrocarbon production—have typically larger uncertainties and vary from approximately -4 to 4 mm/year. Vertical position estimates are about three times less accurate than horizontal position estimates, due primarily to the geometry of the satellite-receiver system relative to the Earth's atmosphere. Vertical positions are also more sensitive to hydrological processes and anthropogenic activity that tend to overprint the vertical displacement that would be expected from an extensional tectonic regime (e.g., Borsa et al., 2014). Thus, care must be taken when evaluating vertical velocities for long-term tectonic deformation. Sites that have an absolute value of vertical rate greater than 1 mm/year are omitted from the strain rate and Euler pole analyses (see section 2.1).

3.2. Profile-Parallel Strain Rates

Five east-west velocity profiles (Figure 3a) are shown below (Figures 5 and 6) with linear weighted least squares regressions fitting all data east of the western boundary of the CP. The slope of each regression indicates the strain rate along that distance. It can be seen that strain rate across central Colorado is very low (-0.41 ± 0.08 nε/year). There is an increase to 0.87 ± 0.07 nε/year in southern Colorado and largest in northern New Mexico (1.26 ± 0.06). Strain rates slightly decrease in central and southern New Mexico down to approximately 0.9 ± 0.08 nε/year.

The assumption of uniform strain rates over the entire region east of the Basin and Range may be an oversimplified model however. There are clear deviations from a simple linear trend in each of the profiles. To test whether the strain rates vary significantly along each profile, we performed weighted linear regressions on segments fitting data west, inside, and east of the major basin-bounding Quaternary faults of the RGR (Figure 6). The eastern-bounding faults defining the RGR are the Williams Fork Mountains fault, Northern Sangre de Cristo fault, Southern Sangre de Cristo fault, Hubbell Springs fault, and Alamogordo fault for profiles 1–5, respectively. In profiles 1 and 2, we simply fit data to the east and west of the RGR, as there is not a strong rift expression or sites within the basin bounding faults. Strain rate in both segments remains nearly zero across the majority of central Colorado with the additional segment. In all four other profiles, the extensional strain rate is significantly higher to the west of the RGR than to the east. For example, in profile 4 the strain rate east of the RGR is 0.72 ± 0.14 nε/year, whereas the strain west of the RGR is 1.83 ± 0.78 nε/year. Strain rates within the RGR are in all cases much larger than outside. Two of the sites thought to be affected by the SMB were not omitted from the analysis based on our criteria and may be responsible for some of the anomalously high strain rate found within the RGR in profile 4.

F test results from the segmented regression tests (Figure 6) suggest that there are variations in strain rate across the RGR. In the cases of profiles 1 and 2, which have no constraints within the basin-bounding faults, the improvement by adding the additional segments is not statistically significant at the 95% confidence level (Table 1), and there is clearly less variation visible. Profile 3 has clear variations within the rift; however, the *p* value for a three-segment model is not significant at the 95% confidence level. However, the two data points in the eastern part of the basin-bounding faults largely control this result. If we were to label these two eastern sites as east of the RGR, the three-segment model is, in fact, significant at the 95% confidence level, but we prefer to leave it as is for consistency. The improvement in profile 4 is significant at the 95% confidence level, and the improvement in profile 5 is significant at the 94% confidence level. Further eliminating noisy sites in Texas brings profile 5 to 95% confidence. In summary, profiles 1 and 2 are best represented by a single regression, whereas profiles 4 and 5 are better represented by three regressions. Profile 3 is more complicated, but we can speculate that the edge effect from the CP may be controlling strain accumulation more than the traditional

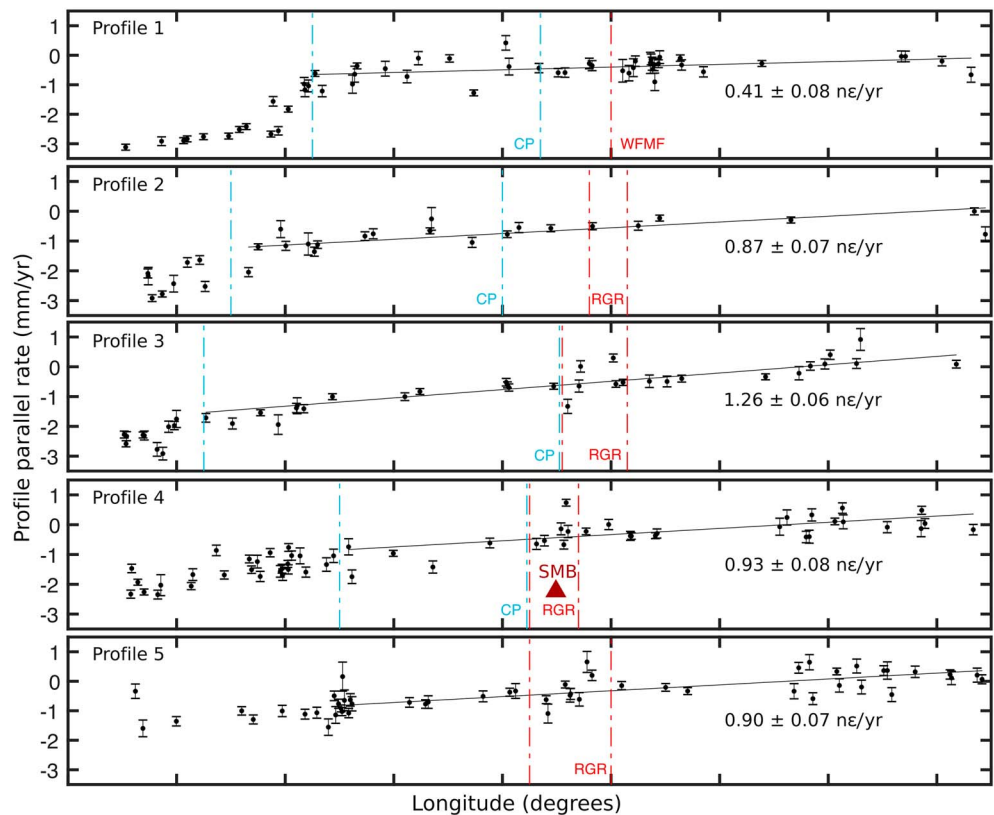


Figure 5. Horizontal Global Positioning System velocities projected onto five profiles (see Figure 3) as a function of longitude. Each profile shows stations within 90 km of the line. Approximate boundaries of the Colorado Plateau (CP) and Rio Grande Rift (RGR) are indicated by blue and red dashed lines, respectively. Boundary of RGR is defined by basin-bounding faults to the east and basin borders to the west (Figure 3). CP boundaries are defined by the longitude where the profile crosses the CP border (Figure 3). WFMF denotes Williams Fork Mountain Fault. Red triangle shows the approximate location of the Socorro Magma Body (SMB) on profile 4. East-west strain rates east of the Basin and Range province and into the Great Plains are estimated in each profile; 1 nε/year is equal to one part per billion (10^9) per year.

RGR basin-bounding faults in this area. Thus, the northern RGR is consistent with a uniform strain-rate across this zone, and sections in the central and southern RGR have significant, but complex, spatial variations in strain-rate.

3.3. Strain Rate Field

Similar to results from the velocity profile strain analysis, we find using a two-dimensional strain rate field (Figure 7) that extensional strain rate is higher within and to the west of the fault-defined RGR than it is to the east in the Great Plains. Extensional strain rates are near zero to the east of the RGR in the Great Plains. Inside and just west of the RGR, strain rates reach up to 10 nε/year (Figure 7b). Strain rates are greater than 10 nε/year in the Basin and Range and the northwest part of the CP. We also observed higher concentrations of strain rate near the central RGR and southeast margin of the CP—partly following the trend of the Jemez lineament. Maximum extensional strain rate and maximum shear strain rate yield similar general patterns. Maximum shear strain rate is pronounced around the entire margin of the CP (Figure 7c), whereas the extensional strain rate is limited to the central RGR, Jemez lineament, and Basin and Range province. Shear strain is particularly high near the Jemez lineament, which is consistent with rotation of the CP relative to the surrounding crust. There is also an anomalously high concentration of dilatational strain associated with the SMB (Figure 7a). This is largely controlled by two sites on the eastern margin of the SMB and would be expected for a magmatic inflation signal. The other sites affected by the SMB were omitted from the

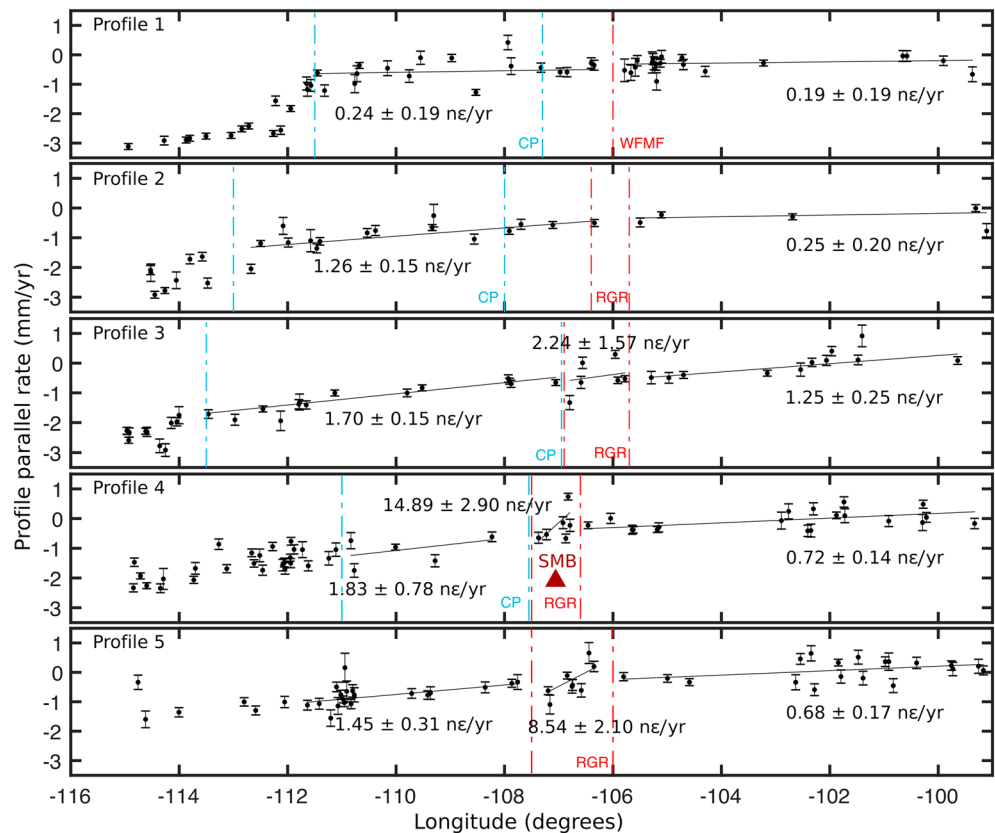


Figure 6. Same as Figure 5 but with segmented strain rate fit to sites west, east, and inside of the major Rio Grande Rift (RGR) basin-bounding Quaternary faults (red dashed lines) where applicable.

analysis but can be seen in Figure 4. Including these sites would make the anomalous SMB strain rate more prominent and constrain it more to the bounds of the known deformation.

3.4. Euler Pole

Previous studies on the RGR have hypothesized that a Euler pole model could be used to characterize the rift opening mechanism, in which a rigid CP rotates clockwise about a Euler pole located to the north (e.g., Cordell, 1982; Chapin et al., 1994). This has been proposed as a driving force for the onset of volcanism at the Jemez lineament and extension of the RGR as the thick rigid CP separates from the thinner crust of the RGR to the southeast (Cordell, 1982; Chapin et al., 1994). This conceptual model implies a progression of rifting from south to north with greater extension rates to the south—which has been used to explain the generally larger basin widths and lower elevations in the southern RGR relative to the north (Cordell, 1982). More recent studies, however, have found little evidence for such a progression and instead show that much of the initiation and evolution of the RGR was synchronous (Landman & Flowers, 2013; Ricketts et al., 2016). Euler pole locations that have been inferred using various geological features result in a wide range of locations spanning northern New Mexico (Muehlberger, 1979; Woodward, 1977), northern Colorado (Cordell, 1982; Zoback & Zoback, 1980), to south central Canada (Eaton, 1979). Chapin et al. (1994) built upon previous estimates, and using previously published extension estimates in the rift, orientations of RGR accommodation zones, orientations of faults bounding isolated rift basins in Colorado and Wyoming, and observations of approximately north-south shortening across the northwestern plateau boundary, suggested that a Miocene Euler pole existed in northeastern Utah (110°W , 40°N), with a clockwise rotations of $1\text{--}1.5^{\circ}/\text{Ma}$. More recent studies have addressed this topic using GPS data but, within the uncertainties of their data, found no clear relationship between CP rotation and RGR opening (Berglund et al., 2012; Kreemer et al., 2010). However, these studies used short GPS time series (2–4 years) and sparse networks (<15 sites within the CP).

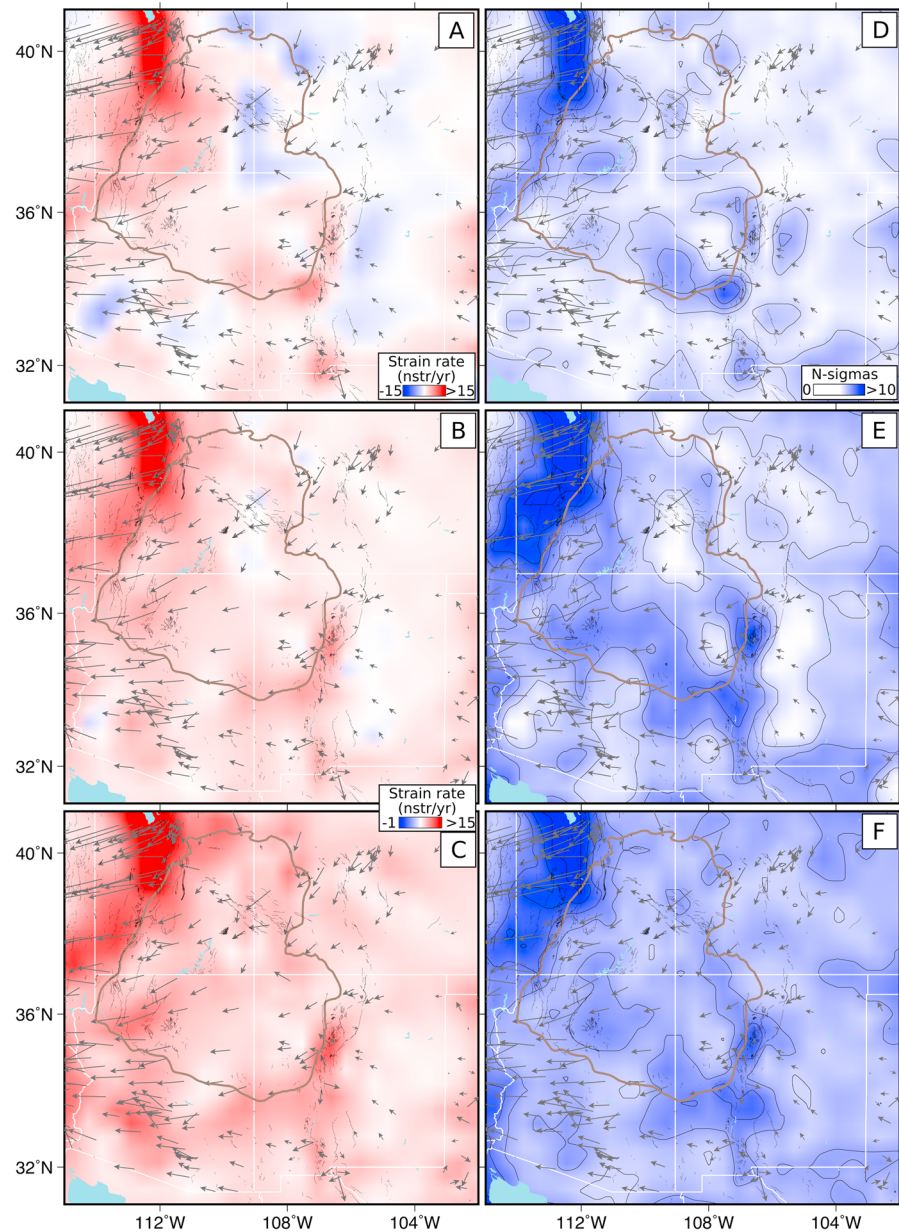


Figure 7. Strain rate maps with Colorado Plateau outlined in brown. (a) First invariant of the strain rate tensor (dilatation). (b) First eigenvalue of the strain rate tensor (maximum extension). (c) Difference between maximum and minimum principal strain rates (maximum shear strain rate). Color bar for panel (c) also applies to panels (a) and (b). (d, e) N -sigmas corresponding to (a), (b), and (c) respectively. 2-sigma contours are plotted in black. N -sigma values greater than 2 are above the 95% confidence level.

Our strain rate analysis resulted in particularly elevated shear strain rates on the southeastern edge of the CP (Figure 7c) as would be expected from clockwise rotation of the CP (Figure 8). Given this result, and the wide interest in CP rotation as it relates to the rigidity of the CP itself and RGR rifting, we provide an updated Euler pole estimate using the additional GPS sites and updated time series now available. The rotation rates we obtained range between -0.0434° and $-0.0178^\circ/\text{Ma}$. The geographic locations of the trial poles, shown in Figure 8, lie within an elliptical region (95% confidence) near the US-Canadian border that is elongated in the direction of the CP, reflecting the limited spatial extent of the CP stations along that direction. The optimal model has a pole relative to NA12-defined stable North America located at 116.946°W , 52.262°N , with a rotation rate of $-0.030 \pm 0.013^\circ/\text{Ma}$ (clockwise, 95% confidence; Figure 8).

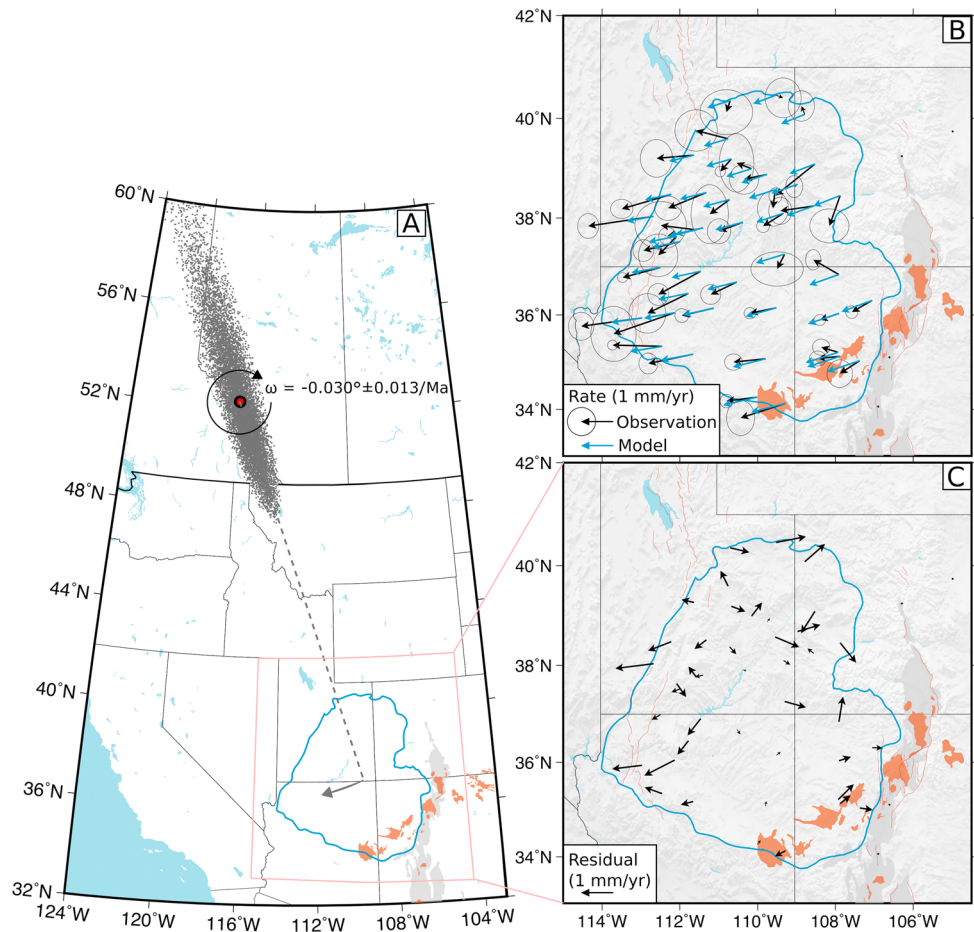


Figure 8. Euler pole results from the inversion of all sites within the physiographic boundaries of the Colorado Plateau (CP). (a) Schematic map of CP rotation with a sample of Euler pole locations (gray dots) defining a 95% confidence region resulting from Monte Carlo simulations. Red circle indicates the optimal Euler pole location. (b) Black vectors represent measured velocities with 95% confidence ellipses at each station, and blue vectors are calculated velocities using the optimal Euler parameters. (c) Residual vectors (observations subtracted from vectors derived from forward model) showing internal deformation within the CP. (a–c) CP outlined in blue, Neogene volcanics in orange, and RGR basins in dark gray.

The optimal model has a weighted RMS misfit of 0.36 mm/year and a normalized root mean square of 2.68, which is significantly higher than the value of 1.0 expected when the misfit is consistent with the data uncertainties. The velocity residuals of the optimal model show a systematic difference between the sites on the east and west of the CP (Figure 8c), suggesting that the CP is internally deforming. To assess this possibility, we divided the CP stations into the 17 stations west and 26 stations east of 110.75°W. Given the poor spatial extent of stations, we fixed the pole location to the optimal model and found by forward modeling that rotation rates of 0.044° and 0.023°/Ma produced the lowest normalized root mean square for the west and east sets, respectively. Thus, the western CP on average is rotating nearly twice as fast as the eastern CP relative to stable North America. If the internal deformation is assumed to be concentrated across a narrow zone along 110.75°W, the east-west differential motion across the zone in the center of the CP would be ~0.65 mm/year. The large scatter and uncertainties in the current data set limit our ability to assess alternative models, such as ones with more uniformly distributed internal deformation.

4. Discussion

4.1. Strain Rate Concentrations

There are measurable strain rate elevations across the central and southern part of the RGR—with the highest concentrations primarily along the southeast margin of the CP. There is no detectable east-west

extensional strain rate in the majority northern RGR where basins become narrower and the characteristic normal fault-bounded half grabens become almost indistinguishable. Strain rates across the RGR range from ~ 1 to 15 ne/year , which is equivalent to a range of ~ 0.1 to 1.5 mm/year of rift opening. This spans and mostly exceeds the estimated range of average historical extension rates across the RGR, which is estimated to be between 0.2 to 0.6 mm/year (Kluth & Schaftenaar, 1994; Ricketts et al., 2014, 2016; Russell & Snelson, 1994). Ricketts et al. (2014) found Quaternary fluid-accelerated extensional strain rates of nearly 100 ne/year calculated from vein opening in the Albuquerque basin. Although our GPS observations do not have the fine spatial resolution required to measure extension comparable to the scale of their measurements, the locations of our observed peak extension rates (Figure 6, profile 4; Figure 7) are consistent with the location of their observations. This area is also near the SMB, which could have an influence on the measurements. The RGR is thought to have undergone historical periods of accelerated rifting (e.g., van Wijk et al., 2018) and changes from magma-dominated extension to tectonic/faulting-dominated extension with periods of quiescence (Ebinger et al., 2013). Taking these variations into consideration, historical extension rates have been estimated to be between ~ 0.1 and 1.1 mm/year for the San Luis and Albuquerque basins (van Wijk et al., 2018). These estimates integrate multiple earthquake cycles for a long-term average. Given that our measurements are only measuring a small window of interseismic strain accumulations, even by the most conservative standards our measurements suggest that much of the RGR remains at least as active as the geologic record indicates.

4.2. Tectonic Behavior

Rift zone characteristics observed throughout the Earth are relatively variable in nature and so are the models used to describe them. Characteristics of rift development depend on many factors, including the structure of the crust (weaknesses and heterogeneities), as well as thermal characteristics and structure of the underlying mantle. From a geodetic perspective, there are typically two end-member models used to describe how continental crust breaks apart: (1) the “diffuse model,” in which extension is accommodated evenly along the principle axis of stress acting on the crust, and (2) the “block model,” in which extension is accommodated in discrete zones along faults (e.g., Thatcher, 2009). The block model approaches diffuse characteristics in the limit of defining an increasing number of “blocks” or faults in the crust—roughly analogous to the domino and large-scale footwall collapse end-member models in structural geology literature. We observe large strain localizations preferentially across the eastern large-offset basin-bounding faults of the RGR (Figures 5 and 6, profiles 4 and 5)—consistent with flexural cantilever models for half-graben basins that have the majority of strain along the large offset border fault, with intrabasin faulting accommodating collapse (e.g., Kuszniir & Ziegler, 1992). Our evidence for strain localization may suggest a degree of block-like behavior at least at the spatial and temporal scales of our observations, but recurrence intervals for large earthquakes in the RGR are orders of magnitude longer than the time scale of geodetic measurements (Machette, 2000; Personius et al., 1999), making it unrealistic to accurately define block models. In an ideal case, we would have geodetic measurements spanning a minimum of one earthquake cycle for each fault in our study area to fully characterize the deformation behavior. Instead, our measurements capture only a small fraction of the interseismic behavior of the rifting process. Strain rate concentrations we observe are thus related to interseismic strain accumulation and/or magmatic-driven stresses. Earthquakes recorded near the RGR within the geodetic timescale (~ 30 years) are small and do not cluster in discrete zones (Sanford et al., 2002) as is predicted by a block model. The exception is the Socorro Seismic Anomaly, which shows strong clustering of low magnitude seismicity above the SMB (Balch et al., 1997; Figure 4).

4.3. Strain Localization at the Jemez Lineament

The most prominent strain rate concentrations in our study area are located near the Jemez lineament. Generally, mantle thinning tends to occur across relatively broad zones, and it may have both horizontal and vertical strain components (e.g., Coblenz et al., 2011; Mahatsente, 2017; van Wijk et al., 2008), but studies of other rifting environments, such as the Ethiopian Rift, suggest when magma rises to crustal levels, strain may localize to the zone of magma intrusion (e.g., Bendick et al., 2006; Bilham et al., 1999; Ebinger & Casey, 2001; Keir et al., 2006). Numerical modeling work has shown horizontal mantle shearing across a lithospheric step, as in the CP boundary, can result in induced decompression melting and excite shear-driven upwelling (Ballmer et al., 2015; Rudzitis et al., 2016). Other work shows active surface uplift from mantle upwelling can drive further lithosphere extension and rifting (Burov & Guillou-Frottier, 2005),

which can cause localized rift acceleration. Recent work supports this model, showing evidence for Quaternary uplift above the Jemez lineament and margins of the CP (Channer et al., 2015; Karlstrom et al., 2012; Levander et al., 2011; Nereson et al., 2013, where the most recent volcanic fields, most of which are younger than 10 Ma and constitute the Jemez lineament, are situated at the southeastern edge of the CP and intersects the RGR obliquely (Figure 1). Based on recent (<5 ma) geologic features, Aldrich (1986) proposed that the Jemez lineament marks a geophysical boundary of the CP. There is also evidence that at approximately 10 and 5 Ma, the least principal horizontal stress orientation rotated from east-west to be oriented perpendicular to the fault strikes along the Jemez lineament (Chapin et al., 2004; Eaton, 1979; Zoback et al., 1981). An updated stress field map, based on formal inversions of focal mechanisms, shows a clear transition in minimum horizontal compression orientation across the Jemez lineament from primarily east-west in the RGR to north-south within the CP (Levandowski et al., 2018). A transition in other geophysical characteristics has been observed in magnetotelluric, gravity, and tomographic (e.g., Karlstrom et al., 2012). Volcanism and elevated seismicity has likely been influenced by CP edge-driven convection, decompression melting, and shear-driven upwelling and coincides with the area where we observe the highest concentrations of elevated strain rate near the RGR, including the distinct uplift and radial deformation from the SMB situated just southeast of the Jemez lineament.

5. Deformation Within the CP

Both vertical and horizontal GPS observations suggest significant deformation within the CP. We find evidence for uplift near the northeast margin (Figure 3b) and strain localizations at various locations along all margins (Figure 7). We were unable to find a Euler pole that could characterize rigid-body rotation of the CP and instead find notable east-west extension (section 3.4; Figure 8). These results are in general agreement with studies suggesting internal deformation due to dynamic topography driven by variable asthenospheric upwelling, lithospheric delamination, and/or magmatic inflation (e.g., Channer et al., 2015; Crow et al., 2014; Donahue et al., 2013; Karlstrom et al., 2008, 2012; Levander et al., 2011; Nereson et al., 2013). Any unmodeled postseismic deformation from nearby earthquakes—particularly from the 2010 El Mayor-Cucapah earthquake—may also have an effect on inferred long-term deformation rates (e.g., Holland et al., 2013; Kreemer et al., 2015). Further work is required to account for these effects.

6. Conclusions

Broad diffuse deformation across an approximately 800–1,200-km area is likely not the optimal statistical representation of the tectonic behavior across the RGR. East-west velocity profiles (Figures 5 and 6) and two-dimensional strain rate field calculations (Figure 7) both suggest strain rates are greater within and directly to the west of the fault-defined RGR than they are to the east, along much of the RGR. However, these strain rate variations are not concentrated completely within the RGR basins and faults. Rather, there are more distinct concentrations of strain rate near the Jemez lineament at the southeastern margin of the CP (Figure 7). This area marks a transition of various geophysical characteristics and coincides with much of the most recent volcanic activity in our study area (Figure 1). This transition likely represents a weakness in the Earth's crust or heterogeneity in the lithosphere and is present in our GPS observations. Magmatism likely resulted from related edge effects, and some of the deformation that was previously accommodated by extension of the RGR may have shifted to be accommodated at the weakened Jemez lineament. Finally, we found that simple rigid-body rotation is not a model that can characterize the CP. There is significant deformation along the CP's margins as well as evidence for internal east-west extension.

The unique features discovered in our velocity and strain rate analysis add to our understanding of the present-day tectonic characteristics of the RGR and CP. More conclusive interpretations will require future analyses of data from the continually expanding network of reliable GPS instruments, further separation of anthropogenic signals from magmatic and tectonic signals, and support from other geophysical and geological data sets.

References

- Aldrich, M. J. (1986). Tectonics of the Jemez lineament in the Jemez Mountains and Rio Grande rift. *Journal of Geophysical Research*, *91*(B2), 1753–1762.
- Argus, D. F., Fu, Y., & Landerer, F. W. (2014). Seasonal variation in total water storage in California inferred from GPS observations of vertical land motion. *Geophysical Research Letters*, *41*, 1971–1980. <https://doi.org/10.1002/2014GL059570>

Acknowledgments

We thank UNAVCO for collecting GPS data in the Earthscope Plate Boundary Observatory, the NGS for supporting the CORS cooperative network, and the University of Nevada Reno for managing the MAGNET network and processing the GPS data. We thank UNAVCO for archiving data from these networks, and the Colorado Plateau, Soil Moisture, Idaho National Laboratory, Northern and Southern Basin and Range, Rio Grande Rift, Socorro Magma Body, SuomiNet, Wasatch, Yellowstone Hotspot, and Yucca Mountain GPS networks (DOI attributions provided in the supporting information). We also thank AZGPS, Leica SmartNet North America, Las Vegas Valley Water Dept., Mesa County Colorado, Texas Dept. of Transportation, Utah TURNGPS, the U. S. Coast Guard, and other agencies for sharing data (attributions provided in the supporting information). GPS time series and velocities used in this paper can be found at <http://geodesy.unr.edu/>. GPS velocity tables are also available as supporting information. Direct research support for this project came from the NSF EarthScope program for the project “Rio Grande Rift II—Kinematics and Dynamics of Continental Deformation in Low Strain-Rate Environments” (NSF EAR 1053596 and 1053597). All maps were drawn partly with the Generic Mapping Tools software (Wessel & Smith, 1998). Finally, we would like to thank Jolante van Wijk and Gary Axen for valuable discussion and support, Corne Kreemer for constructive comments, as well as Cindy Ebinger, Karl Karlstrom, and Associate Editor Mike Poland for their insightful reviews that substantially improved this manuscript.

- Argus, D. F., & Gordon, R. G. (1996). Tests of the rigid-plate hypothesis and bounds on intraplate deformation using geodetic data from very long baseline interferometry. *Journal of Geophysical Research*, *101*(B6), 13,555–13,572. <https://doi.org/10.1029/95JB03775>
- Atwater, T., & Stock, J. (1998). Pacific-North America plate tectonics of the Neogene southwestern United States: An update. *International Geology Review*, *40*(5), 375–402. <https://doi.org/10.1080/00206819809465216>
- Balch, R. S., Hartse, H. E., Sanford, A. R., & Lin, K. W. (1997). A new map of the geographic extent of the Socorro mid-crustal magma body. *Bulletin of the Seismological Society of America*, *87*(1), 174–182.
- Baldrige, W. S., Keller, G. R., Haak, V., Wendlandt, E., Jiracek, G. R., & Olsen, K. H. (2006). The Rio Grande Rift. In *Developments in geotectonics* (Vol. 25, pp. 233–XIII). Elsevier.
- Ballmer, M. D., Conrad, C. P., Smith, E. I., & Johnsen, R. (2015). Intraplate volcanism at the edges of the Colorado Plateau sustained by a combination of triggered edge-driven convection and shear-driven upwelling. *Geochemistry, Geophysics, Geosystems*, *16*, 366–379. <https://doi.org/10.1002/2014GC005641>
- Bendick, R., McClusky, S., Bilham, R., Asfaw, L., & Klemperer, S. (2006). Distributed Nubia-Somalia relative motion and dike intrusion in the Main Ethiopian Rift. *Geophysical Journal International*, *165*(1), 303–310. <https://doi.org/10.1111/j.1365-246X.2006.02904.x>
- Berglund, H. T., Sheehan, A. F., Murray, M. H., Roy, M., Lowry, A. R., Nerem, R. S., & Blume, F. (2012). Distributed deformation across the Rio Grande rift, Great Plains, and Colorado plateau. *Geology*, *40*(1), 23–26. <https://doi.org/10.1130/G32418.1>
- Bertiger, W., Desai, S. D., Haines, B., Harvey, N., Moore, A. W., Owen, S., & Weiss, J. P. (2010). Single receiver phase ambiguity resolution with GPS data. *Journal of Geodesy*, *84*(5), 327–337. <https://doi.org/10.1007/s00190-010-0371-9>
- Bilham, R., Bendick, R., Larson, K., Mohr, P., Braun, J., Tesfaye, S., & Asfaw, L. (1999). Secular and tidal strain across the Main Ethiopian Rift. *Geophysical Research Letters*, *26*(18), 2789–2792. <https://doi.org/10.1029/1998GL005315>
- Blewitt, G., Hammond, W. C., & Kreemer, C. (2009). Geodetic constraints on contemporary deformation in the Northern Walker Lane: 1, Semi-permanent GPS strategy, in Late Cenozoic structure and evolution of the Great Basin–Sierra Nevada transition, edited by J. S. Oldow, and P. H. Cashman. *Geological Society of America Special Papers*, *447*, 1–16.
- Blewitt, G., Kreemer, C., Hammond, W. C., & Gazeaux, J. (2016). MIDAS robust trend estimator for accurate GPS station velocities without step detection. *Journal of Geophysical Research: Solid Earth*, *121*, 2054–2068. <https://doi.org/10.1002/2015JB012552>
- Blewitt, G., Kreemer, C., Hammond, W. C., & Goldfarb, J. M. (2013). Terrestrial reference frame NA12 for crustal deformation studies in North America. *Journal of Geodynamics*, *72*, 11–24. <https://doi.org/10.1016/j.jog.2013.08.004>
- Blewitt, G., Hammond, W. C., & Kreemer, C. (2018). Harnessing the GPS data explosion for interdisciplinary science. *Eos*, *99*. <https://doi.org/10.1029/2018EO104623>
- Borsa, A. A., Agnew, D. C., & Cayan, D. R. (2014). Ongoing drought-induced uplift in the western United States. *Science*, *345*(6204), 1587–1590. <https://doi.org/10.1126/science.1260279>
- Bos, M., Fernandes, R., Williams, S., & Bastos, L. (2013). Fast error analysis of continuous GNSS observations with missing data. *Journal of Geodesy*, *87*(4), 351–360. <https://doi.org/10.1007/s00190-012-0605-0>
- Bos, M. S., Fernandes, R. M. S., Williams, S. D. P., & Bastos, L. (2007). Fast error analysis of continuous GPS observations. *Journal of Geodesy*, *82*(3), 157–166.
- Bürgmann, R., & Thatcher, W. (2013). Space geodesy: A revolution in crustal deformation measurements of tectonic processes. In *The web of geological sciences: Advances, impacts, and interactions*. *Geological Society of America Special Papers*, *500*, 397e430.
- Burov, E., & Guillou-Frottier, L. (2005). The plume head–continental lithosphere interaction using a tectonically realistic formulation for the lithosphere. *Geophysical Journal International*, *161*(2), 469–490. <https://doi.org/10.1111/j.1365-246X.2005.02588.x>
- Cardozo, N., & Allmendinger, R. W. (2009). SSPX: A program to compute strain from displacement/velocity data. *Computers & Geosciences*, *35*(6), 1343–1357. <https://doi.org/10.1016/j.cageo.2008.05.008>
- Channer, M. A., Ricketts, J. W., Zimmerer, M., Heizler, M., & Karlstrom, K. E. (2015). Surface uplift above the Jemez mantle anomaly in the past 4 Ma based on ⁴⁰Ar/³⁹Ar dated paleoprofiles of the Rio San Jose, New Mexico, USA. *Geosphere*, *11*(5), 1384–1400. <https://doi.org/10.1130/GES01145.1>
- Chapin, C. E., Cather, S. M., & Keller, G. R. (1994). Tectonic setting of the axial basins of the northern and central Rio Grande Rift. *Geological Society of America Special Papers*, 5–5.
- Chapin, C. E., Wilks, M., & McIntosh, W. C. (2004). Tectonics, geochronology, and volcanism in the Southern Rocky Mountains and Rio Grande Rift. *New Mexico Bureau of Geology and Mineral Resources Bulletin* 160.
- Coblentz, D., Chase, C. G., Karlstrom, K. E., & van Wijk, J. (2011). Topography, the geoid, and compensation mechanisms for the southern Rocky Mountains. *Geochemistry, Geophysics, Geosystems*, *12*, Q04002. <https://doi.org/10.1029/2010GC003459>
- Cordell, L. (1982). Extension in the Rio Grande rift. *Journal of Geophysical Research*, *87*(B10), 8561–8569.
- Crow, R., Karlstrom, K., Darling, A., Crossey, L., Polyak, V., Granger, D., et al. (2014). Steady incision of Grand Canyon at the million year timeframe: A case for mantle-driven differential uplift. *Earth and Planetary Science Letters*, *397*, 159–173. <https://doi.org/10.1016/j.epsl.2014.04.020>
- DeMets, C., Gordon, R. G., Argus, D. F., & Stein, S. (1994). Effect of recent revisions to the geomagnetic reversal time scale on estimates of current plate motions. *Geophysical Research Letters*, *21*(20), 2191–2194. <https://doi.org/10.1029/94GL02118>
- Donahue, M. S., Karlstrom, K. E., Aslan, A., Darling, A., Granger, D., Wan, E., et al. (2013). Incision history of the Black Canyon of Gunnison, Colorado, over the past ~1 Ma inferred from dating of fluvial gravel deposits. *Geosphere*, *9*(4), 815–826. <https://doi.org/10.1130/GES00847.1>
- Eaton, G. P. (1979). A plate-tectonic model for late Cenozoic crustal spreading in the western United States. In *Rio Grande rift: Tectonics and magmatism* (Vol. 14, pp. 7–32). Washington, DC: American Geophysical Union.
- Ebinger, C. J., & Casey, M. (2001). Continental breakup in magmatic provinces: An Ethiopian example. *Geology*, *29*(6), 527–530. [https://doi.org/10.1130/0091-7613\(2001\)029<0527:CBIMPA>2.0.CO;2](https://doi.org/10.1130/0091-7613(2001)029<0527:CBIMPA>2.0.CO;2)
- Ebinger, C. J., van Wijk, J., Keir, D., & Bickford, M. E. (2013). The time scales of continental rifting: Implications for global processes. *The web of geological sciences: Advances, impacts, and interactions*. *Geological Society of America Special Papers*, *500*, 371–396. [https://doi.org/10.1130/2013.2500\(11\)](https://doi.org/10.1130/2013.2500(11))
- England, P., & McKenzie, D. (1982). A thin viscous sheet model for continental deformation. *Geophysical Journal of the Royal Astronomical Society*, *70*(2), 295–321. <https://doi.org/10.1111/j.1365-246X.1982.tb04969.x>
- Evans, B., & Kohlstedt, D. L. (1995). *Rheology of rocks* (pp. 148–165). Rock Physics & Phase Relations: A Handbook of Physical Constants.
- Fialko, Y., & Simons, M. (2001). Evidence for ongoing inflation of the Socorro magma body, New Mexico, from interferometric synthetic aperture radar imaging. *Geophysical Research Letters*, *28*(18), 3549–3552. <https://doi.org/10.1029/2001GL013318>

- Finnegan, N. J., & Pritchard, M. E. (2009). Magnitude and duration of surface uplift above the Socorro magma body. *Geology*, *37*(3), 231–234. <https://doi.org/10.1130/G25132A.1>
- Gao, W., Grand, S. P., Baldrige, W. S., Wilson, D., West, M., Ni, J. F., & Aster, R. (2004). Upper mantle convection beneath the central Rio Grande rift imaged by *P* and *S* wave tomography. *Journal of Geophysical Research*, *109*, B03305. <https://doi.org/10.1029/2003JB002743>
- Gordon, R. G. (1998). The plate tectonic approximation: Plate nonrigidity, diffuse plate boundaries, and global plate reconstructions. *Annual Review of Earth and Planetary Sciences*, *26*(1), 615–642. <https://doi.org/10.1146/annurev.earth.26.1.615>
- Holland, A. A., Broermann, J., Bennett, R. A., Kreemer, C., & Blewitt, G. (2013). Crustal kinematics of the Colorado Plateau from GPS geodesy, Abstract G41A-0917, Fall Meeting, AGU, San Francisco.
- Hudson, M. R., & Grauch, V. J. S. (2013). *New perspectives on Rio Grande Rift basins: From tectonics to groundwater* (Vol. 494). Geological Society, America.
- Humphreys, E., Hessler, E., Dueker, K., Farmer, G. L., Erslev, E., & Atwater, T. (2003). How Laramide-age hydration of North American lithosphere by the Farallon slab controlled subsequent activity in the western United States. *International Geology Review*, *45*(7), 575–595. <https://doi.org/10.2747/0020-6814.45.7.575>
- Karlstrom, K. E., Coblenz, D., Dueker, K., Ouimet, W., Kirby, E., Van Wijk, J., et al. (2012). Mantle-driven dynamic uplift of the Rocky Mountains and Colorado Plateau and its surface response: Toward a unified hypothesis. *Lithosphere*, *4*(1), 3–22. <https://doi.org/10.1130/L150.1>
- Karlstrom, K. E., Crow, R., Crossey, L. J., Coblenz, D., & Van Wijk, J. W. (2008). Model for tectonically driven incision of the younger than 6 Ma Grand canyon. *Geology*, *36*(11), 835–838. <https://doi.org/10.1130/G25032A.1>
- Keir, D., Ebinger, C. J., Stuart, G. W., Daly, E., & Ayele, A. (2006). Strain accommodation by magmatism and faulting as rifting proceeds to breakup: Seismicity of the northern Ethiopian rift. *Journal of Geophysical Research*, *111*, B05314. <https://doi.org/10.1029/2005JB003748>
- Keller, G. R., & Cather, S. M. (Eds.). (1994). *Basins of the Rio Grande rift: Structure, stratigraphy, and tectonic setting* (Vol. 291). Geological Society of America.
- Kellogg, K. S. (1999). Neogene basins of the northern Rio Grande rift: Partitioning and asymmetry inherited from Laramide and older uplifts. *Tectonophysics*, *305*(1–3), 141–152. [https://doi.org/10.1016/S0040-1951\(99\)00013-X](https://doi.org/10.1016/S0040-1951(99)00013-X)
- Kluth, C. F., & Schaftenaar, C. H. (1994). *Depth and geometry of the northern Rio Grande rift in the San Luis basin, south-central Colorado, Special papers* (pp. 27–27). America: Geological Society.
- Kreemer, C., Blewitt, G., & Bennett, R. A. (2010). Present-day motion and deformation of the Colorado plateau. *Geophysical Research Letters*, *37*, L10311. <https://doi.org/10.1029/2010GL043374>
- Kreemer, C., Blewitt, G., Hammond, W. C., Broermann, J., & Bennett, R. A. (2015). The Geodetic strain rate field for the Colorado Plateau and the southern Basin and Range, Proceedings volume Basin and Range Province Seismic Hazards Summit III, Utah Geological Survey Miscellaneous Publication MP15-5.
- Kusznir, N. J., & Ziegler, P. A. (1992). The mechanics of continental extension and sedimentary basin formation: A simple-shear/pure-shear flexural cantilever model. *Tectonophysics*, *215*(1–2), 117–131. [https://doi.org/10.1016/0040-1951\(92\)90077-J](https://doi.org/10.1016/0040-1951(92)90077-J)
- Landman, R. L., & Flowers, R. M. (2013). (U-Th)/He thermochronologic constraints on the evolution of the northern Rio Grande Rift, Gore Range, Colorado, and implications for rift propagation models. *Geosphere*, *9*(1), 170–187. <https://doi.org/10.1130/GES00826.1>
- Langbein, J. (2012). Estimating rate uncertainty with maximum likelihood: Differences between power-law and flicker-random-walk models. *Journal of Geodesy*, *86*(9), 775–783.
- Langbein, J., & Bock, Y. (2004). High-rate real-time GPS network at Parkfield: Utility for detecting fault slip and seismic displacements. *Geophysical Research Letters*, *31*, L15S20. <https://doi.org/10.1029/2003GL019408>
- Langbein, J., & Johnson, H. (1997). Correlated errors in geodetic time series: Implications for time-dependent deformation. *Journal of Geophysical Research*, *102*(B1), 591–603. <https://doi.org/10.1029/96JB02945>
- Larson, K. M., Freymueller, J. T., & Philipson, S. (1997). Global plate velocities from the Global Positioning System. *Journal of Geophysical Research*, *102*(B5), 9961–9981. <https://doi.org/10.1029/97JB00514>
- Levander, A., Schmandt, B., Miller, M. S., Liu, K., Karlstrom, K. E., Crow, R. S., et al. (2011). Continuing Colorado Plateau uplift by delamination-style convective lithospheric downwelling. *Nature*, *472*(7344), 461–465. <https://doi.org/10.1038/nature10001>
- Levandowski, W., Herrmann, R. B., Briggs, R., Boyd, O., & Gold, R. (2018). An updated stress map of the continental United States reveals heterogeneous intraplate stress. *Nature Geoscience*, *1*.
- Machette, M. N. (2000). Active, capable, and potentially active faults—A paleoseismic perspective. *Journal of Geodynamics*, *29*(3–5), 387–392. [https://doi.org/10.1016/S0264-3707\(99\)00060-5](https://doi.org/10.1016/S0264-3707(99)00060-5)
- MacQueen, J. (1967). *Some methods for classification and analysis of multivariate observations, Proceedings of the Fifth Berkeley Symposium on Mathematical Statistics and Probability* (Vol. 1, pp. 281–297). University of California Press Berkeley and Los Angeles.
- Mahatsente, R. (2017). Global Models of Ridge-Push Force, Geoid, and Lithospheric Strength of Oceanic plates. *Pure and Applied Geophysics*, *174*(12), 4395–4406.
- McCalpin, J. P. (1995). Frequency distribution of geologically determined slip rates for normal faults in the western United States. *Bulletin of the Seismological Society of America*, *85*(6), 1867–1872.
- McCalpin, J. P., Harrison, L. B. J., Berger, G. W., & Tobin, H. (2011). Paleoseismicity of a low-slip-rate normal fault in the Rio Grande rift, USA: The Calabacillas fault, Albuquerque, New Mexico. *Geological Society of America Special Papers*, *479*, 23–46. [https://doi.org/10.1130/2011.2479\(01\)](https://doi.org/10.1130/2011.2479(01))
- Minster, J. B., Jordan, T. H., Molnar, P., & Haines, E. (1974). Numerical modelling of instantaneous plate tectonics. *Geophysical Journal of the Royal Astronomical Society*, *36*(3), 541–576.
- Moucha, R., Forte, A. M., Rowley, D. B., Mitrovica, J. X., Simmons, N. A., & Grand, S. P. (2008). Mantle convection and the recent evolution of the Colorado Plateau and the Rio Grande Rift valley. *Geology*, *36*(6), 439–442. <https://doi.org/10.1130/G24577A.1>
- Muehlberger, W. R. (1979). The Embudo fault between Pilar and Arroyo Hondo, New Mexico: An active intracontinental transform fault. In *Field Conference Guidebook* (pp. 77–72). Socorro, NM: Geol. Soc.
- Nakai, J. S., Sheehan, A. F., & Bilek, S. L. (2017). Seismicity of the rocky mountains and Rio Grande Rift from the EarthScope Transportable Array and CREST temporary seismic networks, 2008–2010. *Journal of Geophysical Research: Solid Earth*, *122*, 2173–2192. <https://doi.org/10.1002/2016JB013389>
- Nereson, A., Stroud, J., Karlstrom, K., Heizler, M., & McIntosh, W. (2013). Dynamic topography of the western Great Plains: Geomorphic and ⁴⁰Ar/³⁹Ar evidence for mantle-driven uplift associated with the Jemez lineament of NE New Mexico and SE Colorado. *Geosphere*, *9*(3), 521–545. <https://doi.org/10.1130/GES00837.1>

- Norabuena, E. O., Dixon, T. H., Stein, S., & Harrison, C. G. (1999). Decelerating Nazca-South America and Nazca-Pacific plate motions. *Geophysical Research Letters*, *26*(22), 3405–3408. <https://doi.org/10.1029/1999GL005394>
- Palano, M., Rossi, M., Cannavò, F., Bruno, V., Aloisi, M., Pellegrino, D., et al. (2010). Etn@ref: A geodetic reference frame for Mt. Etna GPS networks. *Annals of Geophysics*.
- Personius, S. F., Machette, M. N., & Kelson, K. I. (1999). *Quaternary faults in the Albuquerque area—An update*, Geological Society Guidebook (Vol. 50, pp. 189–200). New Mexico: Albuquerque Geology.
- Prescott, W. H., Savage, J. C., & Kinoshita, W. T. (1979). Strain accumulation rates in the western United States between 1970 and 1978. *Journal of Geophysical Research*, *84*(B10), 5423–5435. <https://doi.org/10.1029/JB084iB10p05423>
- Reilinger, R., McClusky, S., Vernant, P., Lawrence, S., Ergintav, S., Cakmak, R., et al. (2006). GPS constraints on continental deformation in the Africa-Arabia-Eurasia continental collision zone and implications for the dynamics of plate interactions. *Journal of Geophysical Research*, *111*, B05411. <https://doi.org/10.1029/2005JB004051>
- Reilinger, R., & Oliver, J. (1976). Modern uplift associated with a proposed magma body in the vicinity of Socorro, New Mexico. *Geology*, *4*(10), 583–586. [https://doi.org/10.1130/0091-7613\(1976\)4<583:MUAWAP>2.0.CO;2](https://doi.org/10.1130/0091-7613(1976)4<583:MUAWAP>2.0.CO;2)
- Ricketts, J. W., Karlstrom, K. E., & Kelley, S. A. (2015). Embryonic core complexes in narrow continental rifts: The importance of low-angle normal faults in the Rio Grande rift of central New Mexico. *Geosphere*, *11*(2), 425–444. <https://doi.org/10.1130/GES01109.1>
- Ricketts, J. W., Karlstrom, K. E., Prievisch, A., Crossey, L. J., Polyak, V. J., & Asmerom, Y. (2014). Quaternary extension in the Rio Grande rift at elevated strain rates recorded in travertine deposits, Central New Mexico. *Lithosphere*, *6*(1), 3–16. <https://doi.org/10.1130/L278.1>
- Ricketts, J. W., Kelley, S. A., Karlstrom, K. E., Schmandt, B., Donahue, M. S., & van Wijk, J. (2016). Synchronous opening of the Rio Grande rift along its entire length at 25–10 Ma supported by apatite (U-Th)/He and fission-track thermochronology, and evaluation of possible driving mechanisms. *Bulletin*, *128*(3–4), 397–424.
- Rudzitis, S., Reid, M. R., & Blichert-Toft, J. (2016). On edge melting under the Colorado Plateau margin. *Geochemistry, Geophysics, Geosystems*, *17*, 2835–2854. <https://doi.org/10.1002/2016GC006349>
- Russell, L. R., & Snelson, S. (1994). Structure and tectonics of the Albuquerque basin segment of the Rio Grande rift: Insights from reflection seismic data. *Geological Society of America, Special Paper*, *291*, 83–112. <https://doi.org/10.1130/SPE291-p83>
- Sandwell, D. T., & Wessel, P. (2016). Interpolation of 2-D vector data using constraints from elasticity. *Geophysical Research Letters*, 1–7.
- Sanford, A. R., Lin, K. W., Tsai, I. C., & Jaksha, L. H. (2002). *Earthquake catalogs for New Mexico and bordering areas: 1869–1998* (Vol. 210, p. 104). New Mexico: Bureau of Geology and Mineral Resources, Circular.
- Savage, J. C. (1983). Strain accumulation in western United States. *Annual Review of Earth and Planetary Sciences*, *11*(1), 11–41. <https://doi.org/10.1146/annurev.ea.11.050183.000303>
- Segall, P., & Davis, J. L. (1997). GPS applications for geodynamics and earthquake studies. *Annual Review of Earth and Planetary Sciences*, *25*(1), 301–336. <https://doi.org/10.1146/annurev.earth.25.1.301>
- Sen, P. K. (1968). Estimates of the regression coefficient based on Kendall's tau. *Japan-America Security Alliance*, *63*(324), 1379–1389. <https://doi.org/10.1080/01621459.1968.10480934>
- Stein, S., & Gordon, R. G. (1984). Statistical tests of additional plate boundaries from plate motion inversions. *Earth and Planetary Science Letters*, *69*(2), 401–412. [https://doi.org/10.1016/0012-821X\(84\)90198-5](https://doi.org/10.1016/0012-821X(84)90198-5)
- Thatcher, W. (2003). GPS constraints on the kinematics of continental deformation. *International Geology Review*, *45*(3), 191–212. <https://doi.org/10.2747/0020-6814.45.3.191>
- Thatcher, W. (2009). How the continents deform: The evidence from tectonic geodesy. *Annual Review of Earth and Planetary Sciences*, *37*(1), 237–262. <https://doi.org/10.1146/annurev.earth.031208.100035>
- Theil, H. (1950). A rank-invariant method of linear and polynomial regression analysis (Parts 1-3). In *Ned. Akad. Wetensch. Proc. Ser. A* (Vol. 53, pp. 1397–1412).
- USGS, Quaternary fault and fold database for the nation (2004). Retrieved from <https://pubs.usgs.gov/fs/2004/3033/fs-2004-3033.html>
- van Wijk, J., Koning, D., Axen, G., Coblentz, D., Gragg, E., & Sion, B. (2018). Tectonic subsidence, geoid analysis, and the Miocene-Pliocene unconformity in the Rio Grande Rift, southwestern United States: Implications for mantle upwelling as a driving force for rift opening. *Geosphere*, *14*(2), 684–709. <https://doi.org/10.1130/GES01522.1>
- van Wijk, J., Van Hunen, J., & Goes, S. (2008). Small-scale convection during continental rifting: Evidence from the Rio Grande rift. *Geology*, *36*(7), 575–578. <https://doi.org/10.1130/G24691A.1>
- Wessel, P., & Smith, W. H. (1998). New, improved version of Generic Mapping Tools released. *Eos, Transactions American Geophysical Union*, *79*(47), 579–579. <https://doi.org/10.1029/98EO00426>
- Williams, S. D. P., Bock, Y., Fang, P., Jamason, P., Nikolaidis, R. M., Prawirodirdjo, L., et al. (2004). Error analysis of continuous GPS position time series. *Journal of Geophysical Research*, *109*, B03412. <https://doi.org/10.1029/2003JB002741>
- Woodward, L. A. (1977). Rate of crustal extension across the Rio Grande rift near Albuquerque, New Mexico. *Geology*, *5*(5), 269–272.
- Zoback, M. L., Thompson, G. A., & Anderson, R. E. (1981). Cainozoic evolution of the state of stress and style of tectonism of the Basin and Range province of the western United States. *Philosophical Transactions of the Royal Society A*, *300*(1454), 407–434. <https://doi.org/10.1098/rsta.1981.0073>
- Zoback, M. L., & Zoback, M. (1980). State of stress in the conterminous United States. *Journal of Geophysical Research*, *85*(B11), 6113–6156.
- Zoback, M. L., & Zoback, M. D. (1989). *Tectonic stress field of the continental United States*, Geophysical Framework of the Continental United States (Vol. 172, pp. 523–539). Boulder, CO: Geological Society of America Memoir. <https://doi.org/10.1130/MEM172-p523>